

On the half-quantized Hall conductance of massive surface electrons in magnetic topological insulator films

Rui Chen^{1,2} and Shun-Qing Shen^{1,*}

¹*Department of Physics, The University of Hong Kong, Pokfulam Road, Hong Kong 999077, China*

²*Department of Physics, Hubei University, Wuhan 430062, China*

(Dated: April 11, 2023)

In topological insulators, massive surface bands resulting from local symmetry breaking are believed to exhibit a half-quantized Hall conductance. However, such scenarios are obviously inconsistent with the Thouless-Kohmoto-Nightingale-Nijs theorem, which states that a single band in a lattice with a finite Brillouin zone can only have an integer-quantized Hall conductance. To explore this, we investigate the band structures of a lattice model describing the magnetic topological insulator film that supports the axion insulator, Chern insulator, and semi-magnetic topological insulator phases. We reveal that the gapped and gapless surface bands in the three phases are characterized by an integer-quantized Hall conductance and a half-quantized Hall conductance, respectively. This result is distinct from the previous consensus that the gapped surface band is responsible for the half-quantized Hall conductance and the gapless band should exhibit zero Hall response. We propose an effective model to describe the three phases and show that the low-energy dispersion of the surface bands inherits from the surface Dirac fermions. The gapped surface band manifests a nearly half-quantized Hall conductance at low energy near the center of Brillouin zone, but is compensated by another nearly half-quantized Hall conductance at high energy near the boundary of Brillouin zone because a single band can only have an integer-quantized Hall conductance. The gapless state hosts a zero Hall conductance at low energy but is compensated by another half-quantized Hall conductance at high energy, and thus the half-quantized Hall conductance can only originate from the gapless band. Moreover, we calculate the layer-resolved Hall conductance of the system. The conclusion suggests that the individual gapped surface band alone does not support the half-quantized surface Hall effect in a lattice model.

I. INTRODUCTION

The half-quantized Hall effect occurs on the topological insulator surface once the surface Dirac fermion acquires a mass due to local symmetry breaking¹⁻⁸ for three reasons: (i) The bulk value of the axion angle $\theta = \pi$ in topological insulators allows either gapless or gapped surface states^{1,3,9-12}. In the gapped case, there must be a half-quantized Hall effect; (ii) The half-quantized Hall effect can be captured by calculating the layer-resolved Hall conductance^{9,11,13-15}; and (iii) The gapped surface state could be described by the massive Dirac equation, which hosts a half-quantized Hall conductance¹⁶⁻²¹. Therefore, it is widely believed that the half-quantized Hall conductance originates from the gapped surface state in magnetic topological insulators²²⁻²⁵. However, there are still concerns for the following reasons: (i) The axion term and (ii) layer-resolved Hall conductance do not guarantee that the half-quantized Hall effect originates from the gapped surface state; (iii) The half quantization in the massive Dirac equation contradicts the common belief that a single band on a two-dimensional finite Brillouin zone can only have an integer-quantized Hall conductance. Moreover, our recent works focus on “parity anomalous semimetals”, in which massive and massless Dirac fermions coexist²⁶⁻²⁸. The half-quantized Hall conductance in the parity anomalous semimetal is attributed to the massless Dirac fermions, rather than the previous consensus that it should be attributed to the massive Dirac fermions. Therefore, how the half quan-

tization is manifested in magnetic topological insulator films is still an open question.

The half-quantized Hall effect is proposed to be realized on magnetically doped topological insulators^{14,22,24,26,29-41} and intrinsic antiferromagnetic topological insulators^{9,18,23,25,42-63}. According to the electronic band structures, the magnetic topological insulator can be divided into three different phases: the semi-magnetic topological insulator phase^{22,26,40} consists of a gapped and a gapless Dirac cone on its top and bottom surfaces [Fig. 1(b)]; the axion^{23,24,33,34,60,61} and Chern^{16,29,30,58-60} insulator phases host two gapped Dirac cones on the top and bottom surfaces [Figs. 1(a) and 1(c)]. Specifically, the gapped Dirac cones on the axion (Chern) insulator phase were believed to be characterized by a half-quantized Hall conductance with the opposite (same) sign on the opposite surface, and they combine to yield a zero (quantized) Hall conductance. However, such scenarios are obviously inconsistent with the Thouless-Kohmoto-Nightingale-Nijs theorem, which states that a single band in a lattice with a finite Brillouin zone can only have an integer-quantized Hall conductance. In the semi-magnetic topological insulator phase, the magnetic gap is characterized by a half-quantized Hall conductance contributed by the gapped surface. The gapless surface is believed to exhibit no effect on the total Hall conductance. In the past years, the three phases have received enormous attention. The axion insulator possesses a unique electromagnetic response from the massive Dirac fermions,

which leads to the quantized topological magnetoelectric effect^{13,64–68}. The semi-magnetic topological insulator provides a condensed-matter realization of the parity anomaly and opens the door for experimental realization of the single Dirac fermion^{22,26,40}. The realization of the Chern insulator phase can lead to the development of novel spintronics devices^{29,30}.

In this work, we systematically study the spectrum, probability distribution, and the corresponding Berry curvature distribution in three phases in magnetic topological insulator films, including the axion insulator, Chern insulator, and semi-magnetic topological insulator phases. We explore how the band structures manifest the half-quantized Hall conductance in a lattice model. In the axion and Chern insulator phases, each gapped surface state contributes a nearly half-quantized Hall conductance at low energy near the center of Brillouin zone, but must be compensated by another nearly half-quantized Hall conductance at high energy near the boundary of Brillouin zone, because a single band can only have an integer-quantized Hall conductance in a lattice model according to Thouless-Khomoto-Nightingale-Nijs theorem⁶⁹. In the semi-magnetic topological insulator phase, the gapless state hosts a zero Hall conductance at low energy but must be compensated by another half-quantized Hall conductance at high energy, because the half-quantized Hall conductance can only originate from the gapless state. Moreover, we propose an effective four-band model to depict the three phases. We confirm that the low-energy surface states in these phases inherit from the Dirac fermions. The states at low and high energies always couple in energy scale and they cannot be treated separately. Due to the coupling effect, the exact half quantization is only revealed in the gapless surface state in the semi-magnetic topological insulator phase, but it is not found in the gapped surface state in the axion and Chern insulator phases from the band calculation.

Moreover, we adopt the layer-resolved Hall conductance to study the three phases. The three phases are characterized by distinct patterns of half-quantized surface Hall effect. The results indicate that the half-quantized surface Hall effect is contributed by all the occupied bands, rather than the individual gapped surface bands.

II. MODEL

To carry out numerical studies on the magnetic topological insulator, we consider a tight-binding Hamiltonian on a cubic lattice for an isotropic three-dimensional topological insulator^{16,20,70}

$$\mathcal{H} = \sum_i c_i^\dagger \mathcal{M}_0 c_i + \sum_{i,\alpha=x,y,z} \left(c_i^\dagger \mathcal{T}_\alpha c_{i+\alpha} + c_{i+\alpha}^\dagger \mathcal{T}_\alpha^\dagger c_i \right), \quad (1)$$

where $\mathcal{T}_\alpha = B\sigma_z\tau_0 - i\frac{A}{2}\sigma_x\tau_\alpha$ and $\mathcal{M}_0 = (M - 6B)\sigma_z\tau_0 + \Delta(z)\sigma_0\tau_z$ with the lattice space is taken to be unity.

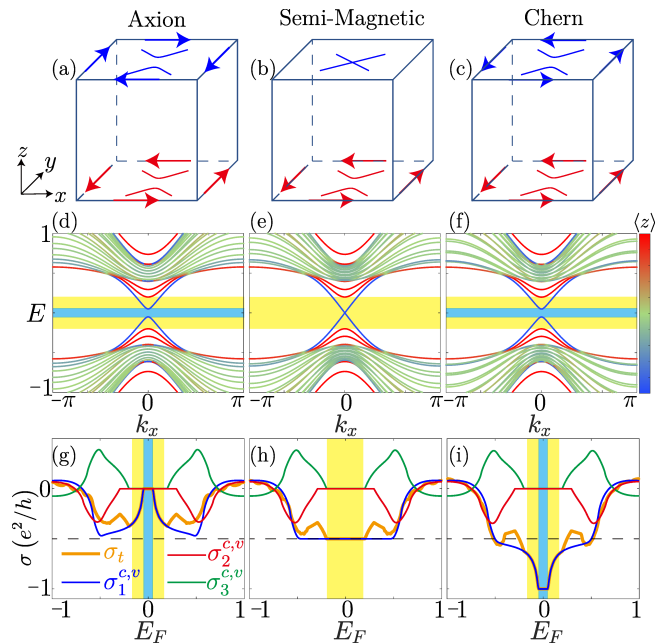


Figure 1. (a) Schematic illustration of the axion insulator phase. The arrows indicate the propagating direction of the surface chiral currents. Blue and red correspond to the top and bottom surfaces, respectively. (d) Energy spectra of the axion insulator phase. Here the color scheme of the bands indicates the wave function distribution. (g) Numerically calculated Hall conductance $\sigma_1^{c,v}$ (blue), $\sigma_2^{c,v}$ (red), $\sigma_3^{c,v}$ (green), and σ_t (orange) as functions of E_F . Here, σ_t depicts the conductance contributed from all the bands, $\sigma_1^{c,v}$ depict the conductance contributed from the lowest conduction and highest valence bands, $\sigma_2^{c,v}$ depict the conductance contributed from the second lowest conduction and second highest valence bands, and so on. The dashed black line corresponds to $\sigma = -e^2/2h$. In (d) and (g), the yellow and light blue regions correspond to the magnetic gap on the top and bottom surfaces, respectively. (b, e, h) and (c, f, i) are the same as (a, d, g), except that they depict the semi-magnetic topological insulator phase and the Chern insulator phase, respectively. We take $\Delta_t = 0.05$ for the axion insulator phase, $\Delta_t = 0$ for the semi-magnetic topological insulator phase, and $\Delta_t = -0.05$ for the Chern insulator phase. The Zeeman splitting term for the bottom surface is $\Delta_b = -0.2$ for all three phases. The film thickness is taken as $n_z = 10$.

Near the $\mathbf{k} = 0$ point in the momentum space (i.e., the low-energy regime), this model is reduced to a Dirac-like model in the absence of the magnetic effect. σ and τ are Pauli matrices. The magnetic effect is represented by layer-dependent Zeeman splitting $\Delta(z)$. We take $\Delta(z) = \Delta_b$ for the bottom surface with $z = 1, 2$, $\Delta(z) = \Delta_t$ for the top surface with $z = n_z - 1, n_z$, and $\Delta(z) = 0$ elsewhere. The axion and Chern insulator phases are characterized by $\Delta_t\Delta_b < 0$ and $\Delta_t\Delta_b > 0$, respectively. The semi-magnetic topological insulator phase is characterized by either $\Delta_b \neq 0$ and $\Delta_t = 0$ or $\Delta_b = 0$ and $\Delta_t \neq 0$. In the subsequent calculations, we fix the parameters as $A = 0.5$, $B = 0.25$, and $M = 0.4$.

When magnetization is introduced to a certain surface, it is believed that the gapless Dirac cone will open an energy gap characterized by a half-quantized Hall conductance, with its sign depending on the magnetization direction. For both Chern and axion insulator phases, the Zeeman effect is introduced to the top and bottom surfaces. Therefore the surface states open energy gaps at the Γ point on both the top and bottom surfaces [Figs. 1(a) and 1(c)]. When the two surfaces have antiparallel magnetization alignment [Fig. 1(a)], the system is characterized by half-quantized Hall conductance with the opposite sign on the opposite surface, leading to the emergence of the axion insulator phase. Because the top and bottom surfaces have parallel magnetization alignment in the Chern insulator phase, the system is characterized by the half-quantized Hall conductance with the same sign [Fig. 1(c)], and they combine to yield a quantized Hall conductance. The semi-magnetic topological insulator phase is characterized by a half-quantized Hall conductance, contributed by the gapped Dirac cone on the magnetic bottom surface [Fig. 1(b)].

However, the above scenarios seem to contradict the common belief that a single band in a lattice model can only host an integer-quantized Hall conductance in units of e^2/h . Next, we study the spectrum and the corresponding probability distribution of the three phases in the lattice model in Eq. (1), and explore how the band structures reconcile the contradiction and how the half quantization is manifested.

III. SPECTRUM AND HALL CONDUCTANCE

The second and third rows in Fig. 1 show the numerically calculated energy spectra and the corresponding Hall conductance for the three phases, respectively. We take $\Delta_b = 0.2$ and $\Delta_t = \mp 0.05$ for the axion and Chern insulator phases and $\Delta_b = 0.2$ and $\Delta_t = 0$ for the semi-magnetic topological insulator phase, respectively. The results are as expected. In the axion insulator phase, the spectrum opens a gap [Fig. 1(d)] characterized by a zero Hall conductance [the orange line in Fig. 1(g)]. The spectrum of the Chern insulator phase [Fig. 1(f)] is the same as the axion insulator phase, except that the gap is characterized by a quantized Hall conductance [the orange line in Fig. 1(i)]. The spectrum of the semi-magnetic topological insulator phase is gapless [Fig. 1(e)], and the system is characterized by a half-quantized Hall conductance when the Fermi energy is located at the magnetic gap of the bottom surface [the orange line in Fig. 1(h)]. Here, the conductance for the m -band is calculated by¹⁹

$$\sigma_m(E_F) = -i\hbar e^2 \sum_{n \neq m} \int \frac{d^2k}{(2\pi)^2} \frac{\langle m | v_x | n \rangle \langle n | v_y | m \rangle}{E_m - E_n} \times \frac{f(E_F - E_n) - f(E_F - E_m)}{E_m - E_n + i\eta}, \quad (2)$$

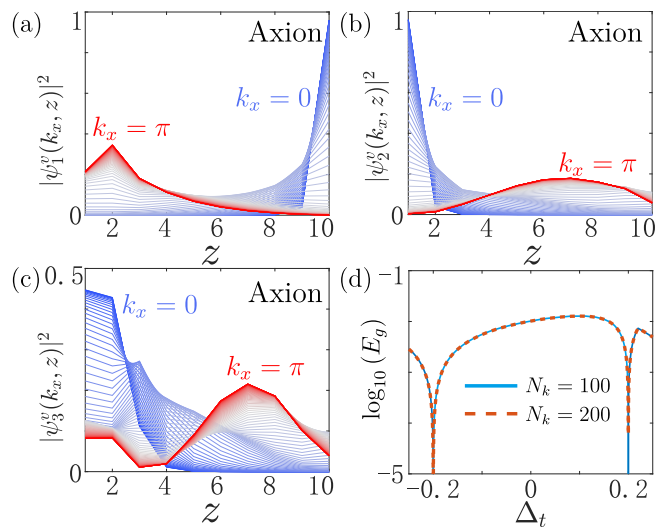


Figure 2. (a) Probability distribution $|\psi_1^v(k_x, z)|^2$ as a function of layer index z for the highest valence band of the axion insulator phase for different k_x . (b) and (c) are the same as (a), except that they depict the second and third highest valence bands. The probability distributions of the semi-magnetic topological insulator phase and the Chern insulator phase are similar to that of the axion insulator phase. (d) The logarithm of the energy gap between the first and second valence bands as a function of Δ_t . Each point is obtained by searching the minimum energy difference between the first and second valence bands by scanning in the two-dimensional Brillouin zone. The k points used in the calculation is $N_k \times N_k$. The Zeeman splitting for the bottom surface is taken as $\Delta_b = -0.2$. The film thickness is $n_z = 10$. In (a-c), we take $\Delta_t = 0.05$.

with $|m\rangle$ is the eigensate of energy E_m for the quasi-2D system confined along the z direction. v_x and v_y are the velocity operators. $f(x)$ is the Fermi distribution and η is an infinitesimal quantity. The total conductance contributed from all the bands has the form $\sigma_t(E_F) = \sum_m \sigma_m(E_F)$.

When the Fermi energy is located at the magnetic surface gaps [the yellow region in Figs. 1(d-f)], the topology nature of the three phases is dominated by the lowest conduction and highest valence bands [see the blue and orange lines in Fig. 1(g-i)]. The higher conduction and lower valence bands exhibit no contribution to the total Hall conductance [the red and green lines in Fig. 1(g-i)].

Figures 2(a-c) show the probability distributions $|\psi_{i=1,2,3}^v(k_x, z)|^2$ of the valence bands as functions of z for different k_x in the axion insulator phase, where ψ_i^v is the wave function distribution of the i -th highest valence band. It is noted that the probability distributions of the semi-magnetic topological insulator phase and Chern insulator phase are similar to that of the axion insulator phase [as shown in Figs. 1(d-f)]. The probability distribution of the highest valence band $|\psi_1^v(k_x, z)|^2$ is mainly distributed at the top surface for the low-energy states near $k_x = 0$ [the blue lines in Fig. 2(a)], and is mainly dis-

tributed at the bottom surface for the high-energy states near $k_x = \pi$ [the red lines in Fig. 2(a)].

The second and third highest valence bands exhibit no contribution to the total Hall conductance when the Fermi energy resides in the magnetic gap. Their probability distributions $|\psi_{2,3}^v(k_x, z)|^2$ are mainly distributed at the bottom surfaces for the low-energy state near $k_x = 0$ [the blue lines in Figs. 2(b) and 2(c)], and are mainly distributed at the bulk for the high-energy state near $k_x = \pi$ [the red lines in Figs. 2(b) and 2(c)]. Moreover, to confirm that the first and second valence bands are well separated in energy scale, we plot $\log_{10}(E_g)$ as a function of Δ_t in Fig. 2(d), where E_g is the minimum energy difference between the first and second valence bands by scanning the whole two-dimensional Brillouin zone. E_g converges with the increasing density of the k points. The results indicate that the first and second valence bands are well separated in energy scale, except at two special points with $\Delta_t = \pm\Delta_b$.

The above scenario indicates that the highest valence band, that dominates the topology of the three phases when Fermi energy resides in the magnetic gap, is localized at one surface at low energy near the Dirac point and at the other surface at high energy near the Brillouin boundary. In contrast to the previous consensus^{13,49,64}, the topology natures of the three phases are dominated by the two surface states near the Γ point.

IV. EFFECTIVE MODEL

The lowest four bands of the magnetic topological insulator thin film can be effectively described by a 4×4 Hamiltonian in the two-dimensional Brillouin zone^{20,26,27,70}:

$$H = \begin{pmatrix} h(\mathbf{k}) + V_t \tau_z & j[m_0(\mathbf{k})/T] m_0(\mathbf{k}) \\ j[m_0(\mathbf{k})/T] m_0(\mathbf{k}) & -h(\mathbf{k}) + V_b \tau_z \end{pmatrix}, \quad (3)$$

where $m_0(\mathbf{k}) = M - 4B(\sin^2 k_x/2 + \sin^2 k_y/2)$, $V_{t/b}(k) = \Delta_{t/b} j[-m_0(\mathbf{k})/T] + \Delta'_{t/b} j[m_0(\mathbf{k})/T]$, and $h(\mathbf{k}) = A(\tau_y \sin k_x - \tau_x \sin k_y)$ describes the massless Dirac fermion. The Fermi-Dirac-distribution like factor $j(x) = [\exp(x) + 1]^{-1}$ describes the process that the surface states merge into the bulk states. $\Delta'_{t/b}/\Delta_{t/b} \simeq n_z^{\text{Mag}}/n_z \ll 1$ where n_z^{Mag} is the thickness of the magnetically doped film. For thick films with a large n_z , we have $\Delta'_{t/b} \rightarrow 0$. The coefficient $T^* = 0.05$ is a model-specific parameter. The first row in Fig. 3 compares the spectra obtained from the numerical tight-binding calculations and the analytical effective models in Eq. (3). The effective Hamiltonian captures the band structures of the three phases in the magnetic topological insulator. Moreover, in the following content, we will show that this effective Hamiltonian also captures the band topologies of the three topological phases.

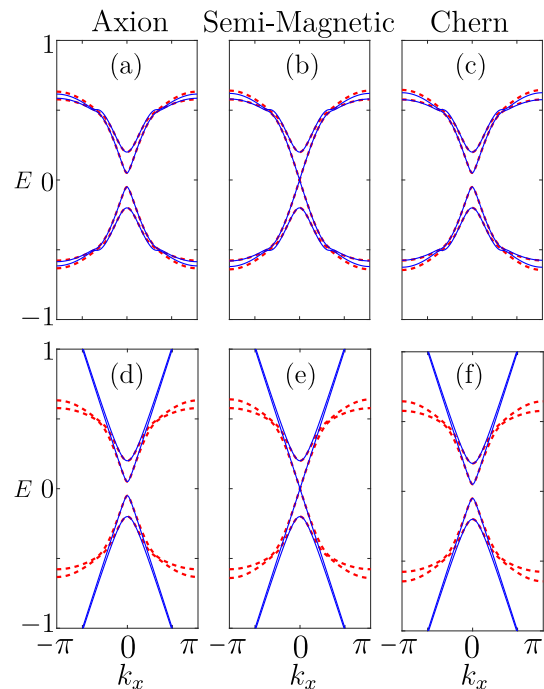


Figure 3. (a, d) Energy spectrum of the axion insulator phase with $\Delta_t = 0.05$ and $\Delta_b = -0.2$. The red dashed lines are obtained by numerical calculations (where only the two lowest conductance and two highest valence bands are illustrated). The solid lines in (a) and (d) are obtained from the effective Hamiltonians in Eqs. (3) and (4), respectively. (b, e) and (c, f) are the same as (a, d), except that they depict (b, e) the semi-magnetic topological insulator phase with $\Delta_t = 0$ and (c, f) the Chern insulator phase with $\Delta_t = 0.05$, respectively.

The Brillouin zone is divided into two regimes by the sign of $m_0(\mathbf{k})$. In the low-energy regime near the center of Brillouin zone, i.e., $k^2 < k_c^2$, we have $j[m_0(\mathbf{k})/T] \rightarrow 0$ and $j[-m_0(\mathbf{k})/T] \rightarrow 1$, where the value of k_c is given by $m_0(\mathbf{k}_c) = 0$. The effective Hamiltonian in Eq. (3) reduces to

$$H = \begin{pmatrix} h'(\mathbf{k}) + \Delta_t \tau_z & 0 \\ 0 & -h'(\mathbf{k}) + \Delta_b \tau_z \end{pmatrix}, \quad (4)$$

with $h'(\mathbf{k}) = A(\tau_y k_x - \tau_x k_y)$. The low-energy effective model describes two decoupled Dirac fermions with the Dirac mass determined by V_t and V_b , respectively. The effective low-energy effective Hamiltonian reproduces the key features of the band structures, that the spectra are dominated by the two decoupled Dirac fermions near the Γ point [the second row in Fig. 3].

In the high-energy regime near the boundary of Brillouin zone, i.e., $k^2 > k_c^2$, we have $j[m_0(\mathbf{k})/T] \rightarrow 1$ and $j[-m_0(\mathbf{k})/T] \rightarrow 0$. The effective Hamiltonian in Eq. (3) reduces to

$$H = \begin{pmatrix} h(\mathbf{k}) + \Delta'_t \tau_z & m_0(\mathbf{k}) \\ m_0(\mathbf{k}) & -h(\mathbf{k}) + \Delta'_b \tau_z \end{pmatrix}. \quad (5)$$

The top and bottom surface states are coupled via the term $m_0(\mathbf{k})$ in the high-energy regime.

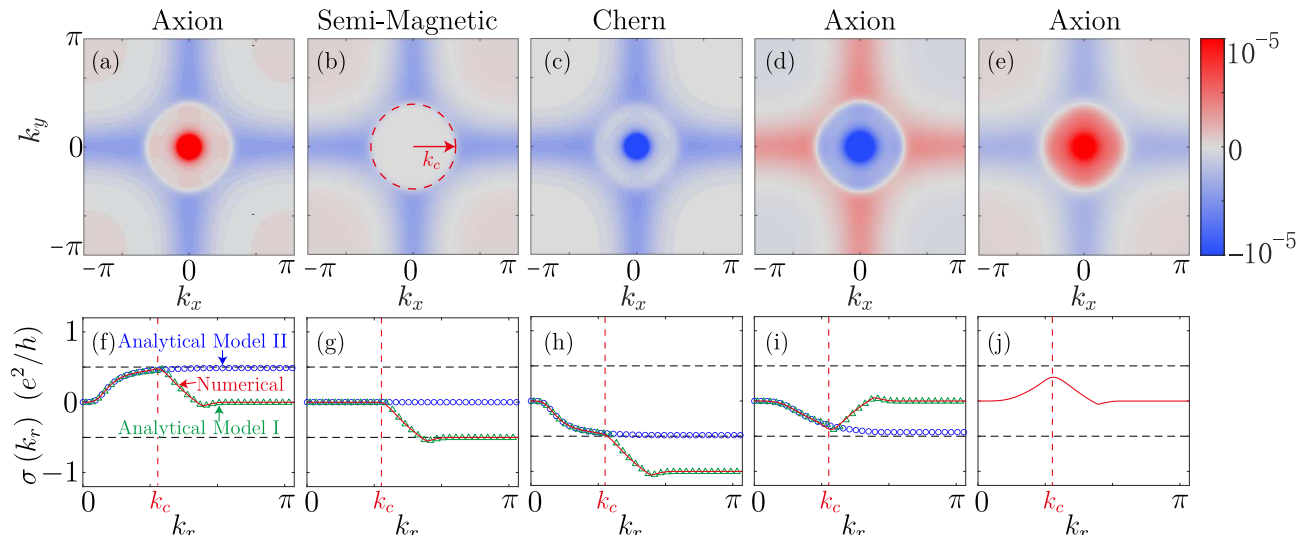


Figure 4. (a) $\Omega_1^v(k_x, k_y)$ as a function of k_x and k_y , where $\Omega_1^v(k_x, k_y)$ corresponds to the Berry curvature of the highest valence band in the axion insulator phase. (f) $\sigma(k_r)$ as a function of k_r . (b, g) and (c, h) are the same as (a, f), except that they depict the semi-magnetic topological insulator and the Chern insulator phase, respectively. The solid red line is obtained by numerical calculations. The blue circle and green triangle points are obtained from the effective Hamiltonians in Eqs. (3) and (4), respectively. The black dashed lines correspond to the half-quantized value with $\sigma_1^v(k_r) = \pm e^2/2h$. The red dashed line corresponds to $k_r = k_c$. (d, i) and (e, j) are the same as (a, f), except that they depict the second and third highest valence bands for the axion insulator phase. The results for the semi-magnetic topological insulator phase and the Chern insulator phase are similar to the axion insulator phase. The parameters are $\Delta_b = -0.2$ and $\Delta_t = 0.05$ for the axion insulator phase, $\Delta_t = 0$ for the semi-magnetic topological insulator phase, and $\Delta_t = -0.05$ for the Chern insulator phase. The film thickness is taken as $n_z = 10$.

V. BERRY CURVATURE DISTRIBUTION

Now, we investigate the Berry curvature distributions and search for the underlying half quantization in the three systems. The first row in Fig. 4 shows the Berry curvature distribution $\Omega(k_x, k_y)$ as a function of k_x and k_y . The Berry curvature distributions exhibit distinct behaviors for $k_r < k_c$ (the low-energy regime) and $k_r > k_c$ (the high-energy regime), where k_r is the radius of the circle centered at the origin in the Brillouin zone and k_c corresponds to the critical radius [see the red circle in Fig. 4(b)]. The second column shows the conductance of the m -th band $\sigma_m(k_r)$ as a function of k_r at $E_F = 0$, where

$$\sigma_m(k_r) = -i\hbar e^2 \times \sum_{n \neq m, k^2 < k_r^2} \int \frac{d^2k}{(2\pi)^2} \frac{\langle m | v_x | n \rangle \langle n | v_y | m \rangle}{E_m - E_n} \times \frac{f(-E_n) - f(-E_m)}{E_m - E_n + i\eta}, \quad (6)$$

Let us focus on the low-energy regime (i.e., $k_r < k_c$). The highest valence band is characterized by $\sigma_1^v(k_c) = 0.47e^2/h$ for the axion insulator phase [Fig. 4(f)], $\sigma_1^v(k_c) = 0$ for the semi-magnetic topological insulator [Fig. 4(g)], and $\sigma_1^v(k_c) = -0.47e^2/h$ for the Chern insulator phase [Fig. 4(h)]. The second and third highest valence bands are characterized by $\sigma_2^v(k_c) = -0.38e^2/h$ [Fig. 4(i)] and $\sigma_3^v(k_c) = 0.35e^2/h$ [Fig. 4(j)] for all

three phases. In the low-energy regime, the calculated Hall conductance from the analytical low-energy effective model in Eq. (4) [the blue circle points in Figs. 4(f)-4(i)] can reproduce the numerically calculated Hall conductance from the tight-binding models [the solid red lines in Figs. 4(f)-4(i)]. This further confirms that, at low-energy regimes, the topologies of the systems are dominated by the Dirac fermions on the top and bottom surfaces.

When the whole Brillouin zone is considered, each band in the axion and Chern insulator phases can only host a quantized Hall conductance, i.e., $\sigma_1^v(\pi) = 0$ for the axion insulator phase [Fig. 4(f)] and $\sigma_1^v(\pi) = e^2/h$ for the Chern insulator phase [Fig. 4(h)]. The gapless band in the semi-magnetic topological insulator is characterized by an exact half-quantized Hall conductance with $\sigma_1^v(\pi) = e^2/2h$ [Fig. 4(g)]. The second and third highest valence bands are characterized by $\sigma_{2,3}^v(\pi) = 0$ for all three phases [Figs. 4(i) and 4(j)].

VI. HALF-QUANTIZED HALL CONDUCTANCE

In previous studies based on the low-energy effective model, the surface states are believed to host a half-quantized Hall conductance when local time-reversal symmetry is broken. However, this is not realizable in a realistic system where each band can only host an integer-quantized Hall conductance. The above scenarios explain how this contradiction is reconciled in a lattice model.

In the axion and Chern insulator phases, the highest valence band is dominated by a nearly half-quantized Hall conductance from one surface at low energy, and must be compensated by another nearly half-quantized Hall conductance from the other surface at high energy. In the semi-magnetic topological insulator phase, the highest valence band is dominated by a zero Hall conductance from one surface at low energy, and is compensated by another half-quantized Hall conductance from the other surface at high energy. This is because the half-quantized Hall conductance can only originate from the symmetry-protected gapless highest valence band, and all the rest bands can only contribute a quantized Hall conductance.

Moreover, due to the coupling between the low-energy and high-energy states, the exact half quantization can not be observed in the axion and Chern insulator phases. As shown in Fig. 4(f), the contribution to the Hall conductance $\sigma(k_r)$ from the low-energy massive Dirac cone (i.e., the blue circle dots) increases with the increasing k_r . The exact half quantization $\sigma(k_r) \rightarrow e^2/2h$ shall be achieved only if $k_r \rightarrow \infty$. However, the high-energy state also contributes to $\sigma(k_r)$ when $k_r > k_c$, which prohibits the observation of the exact half quantization. Thus, only a nearly half quantized Hall conductance $\sigma_1^v(k_c) = 0.47e^2/h$ is observed at $k_r = k_c$. In contrast, the exact half quantization could only be observed in the semi-magnetic topological phase, because its low-energy state does not contribute to the Hall conductance.

VII. LAYER-RESOLVED HALL CONDUCTANCE

The axion insulator phase can be distinguished from the normal insulator phase by calculating the layer-resolved Hall conductance. The layer-resolved Hall conductance of the m -th occupied band is given by^{9,11,13–15}

$$\tilde{\sigma}_m(z) = \frac{e^2}{2\pi h} \int d^2\mathbf{k} \mathcal{F}_{xy}^{mm}(\mathbf{k}, z), \quad (7)$$

where

$$\mathcal{F}_{\alpha\beta}^{mn}(\mathbf{k}) = \partial_\alpha \mathcal{A}_\beta^{mn}(\mathbf{k}) - \partial_\beta \mathcal{A}_\alpha^{mn}(\mathbf{k}) + i [\mathcal{A}_\alpha^{mn}(\mathbf{k}), \mathcal{A}_\beta^{mn}(\mathbf{k})] \quad (8)$$

is the non-Abelian Berry curvature in terms of $\mathcal{A}_\alpha^{mn}(\mathbf{k}, z)$ with the band indexes m and n . The layer-resolved Hall conductance of all occupied bands is given by $\tilde{\sigma}(z) = \sum_{E_m < E_F} \tilde{\sigma}_m(z)$. Moreover, the net Hall conductance of the m -th band and the layer-resolved Hall conductance of the m -th band is connected through $\sigma_m = \sum_{z=1}^{n_z} \tilde{\sigma}_m(z)$.

Figure 5(a) shows $\tilde{\sigma}(z)$ as a function of z for the axion insulator ($\Delta_t = 0.05$), semi-magnetic topological insulator ($\Delta_t = 0$), and Chern insulator phases ($\Delta_t = -0.05$). The bottom surface layers have the same magnetization alignments in the three phases, thus they host the same layer-resolved Hall conductance [$\tilde{\sigma}(z = 1, 2, 3)$ in Fig. 5(a)]. The top surface layers have the opposite magnetization alignments in the axion insulator (green) and

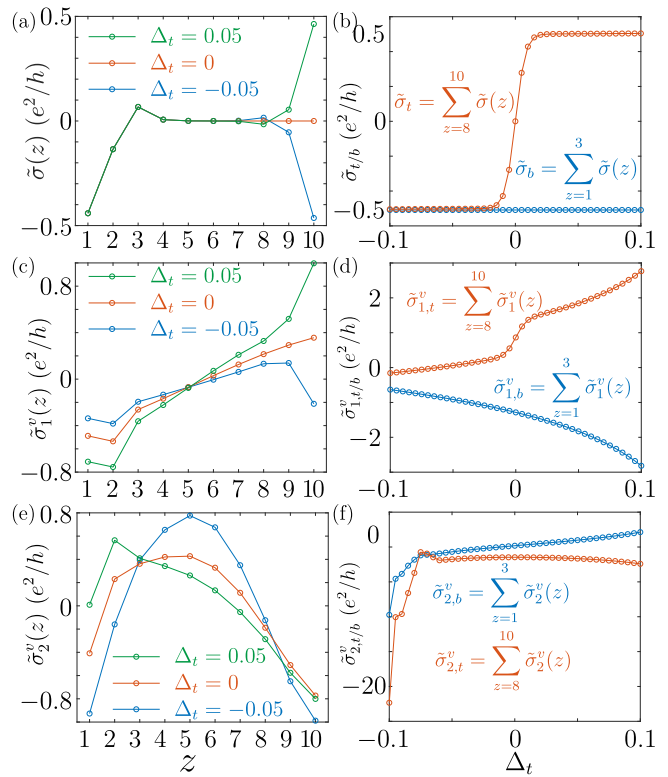


Figure 5. (a) The layer-resolved Hall conductance $\tilde{\sigma}(z)$ as a function of layer z for different Δ_t . Green, red, and blue correspond to the axion insulator ($\Delta_t = 0.05$), semi-magnetic insulator ($\Delta_t = 0$), and Chern insulator phases ($\Delta_t = -0.05$), respectively. (b) $\tilde{\sigma}_{t/b}$ as functions of Δ_t . Here, $\tilde{\sigma}_{t/b}$ depicts the layer-resolved Hall conductance contributed from the top/bottom surface layers. In (a-b), the calculations take into account the contributions from all the occupied bands. (c-d) and (e-f) are the same as (a-b), except that the obtained layer-resolved Hall conductance only takes into account the contributions from the first valence band in (c-d) and from the second valence band in (e-f), respectively. Here, we take the Fermi energy $E_F = 0$, the film thickness $n_z = 10$, and $\Delta_b = -0.2$.

Chern insulator (blue) phases, thus the corresponding layer-resolved Hall conductances have the opposite signs in the two phases [$\tilde{\sigma}(z = 8, 9, 10)$ in Fig. 5(a)]. The top surface layers are non-magnetic in the semi-magnetic topological insulator (red) phase, thus the corresponding layer-resolved Hall conductances is zero. This phenomenon is observed more clearly in Fig. 5(b), where we show $\tilde{\sigma}_{t/b}$ as functions of Δ_t . $\tilde{\sigma}_t = \sum_{z=8}^{10} \tilde{\sigma}(z)$ and $\tilde{\sigma}_b = \sum_{z=1}^3 \tilde{\sigma}(z)$ depict the layer-resolved Hall conductance of the top and bottom surface layers, respectively. With the increasing Δ_t , $\tilde{\sigma}_b$ remains unchanged but $\tilde{\sigma}_t$ increases from -0.5 to 0 and then to 0.5 , which corresponds to the phase crossovers from the Chern insulator phase to the semi-magnetic topological insulator phase and then to the axion insulator phase.

The above calculations take into account the contributions from all the occupied bands and we show that the

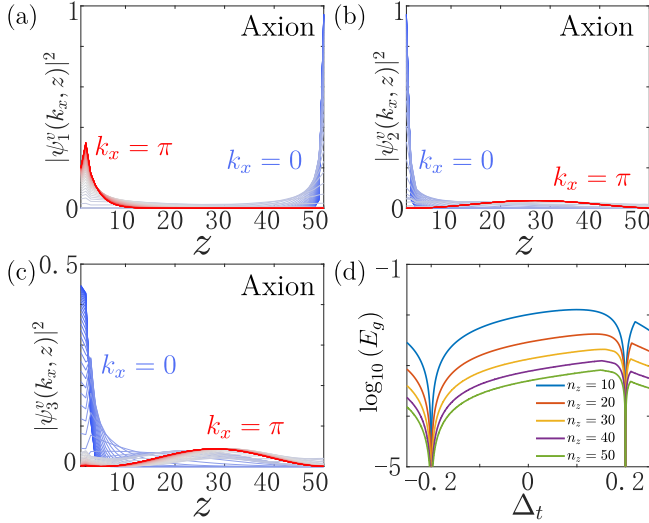


Figure 6. (a) Wave function distribution as a function of layer index z for the highest valence band of the axion insulator phase for different k_x . (b) and (c) are the same as (a), except that they depict the second and third valence bands. The wave function distributions of the semi-magnetic topological insulator phase and the Chern insulator phase are similar to the axion insulator phase. (d) The logarithm of the energy gap between the first and second valence bands as a function of Δ_t for different thicknesses n_z . Each point is obtained by finding the minimum energy difference between the first and second valence bands by scanning in the two-dimensional Brillouin zone. The k points used in the calculation is $N_k \times N_k$, with $N_k = 200$. The parameters are taken as $\Delta_b = -0.2$. In (a-c), we take $\Delta_t = 0.05$ and $n_z = 50$.

half quantization can be extracted in the three phases. However, we find that the half quantization cannot be extracted if only one single band is considered. This is shown in Figs. 5(c-d) and Figs. 5(e-f), which are the same as Figs. 5(a-b), except that the numerically calculated layer-resolved Hall conductance only considers the contributions from the first valence band and the second valence band, respectively. The layer-resolved Hall conductances of one single band have divergent values for each layer. This implies that the half-quantized surface Hall effect is a consequence of all the occupied bands, rather than the individual gapped surface bands.

VIII. DIFFERENT THICKNESS AND PARAMETERS

Above, we consider a thinfilm case with $n_z = 10$. Now, we show that the conclusions are irrelevant to the film thickness. Figures 6(a-c) show the probability distributions of the first, second, and third highest valence bands for different k_x with $n_z = 50$, respectively. The conclusions are similar to the thinfilm case shown in Figs. 2(a-c). Figure 6(d) shows the logarithm of the energy gap between the first and second valence bands as a function

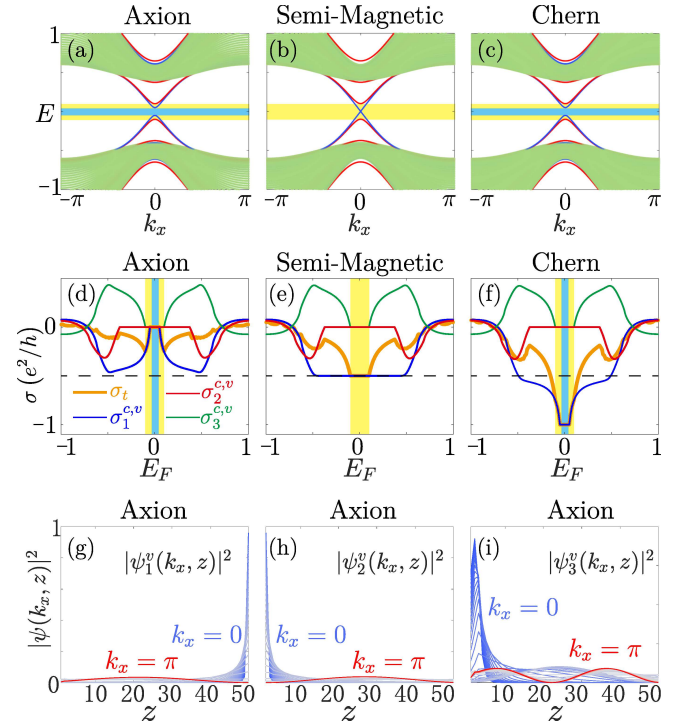


Figure 7. (a) Energy spectra of the axion insulator phase. Here the color scheme of the bands indicates the wave function distribution. (d) Numerically calculated Hall conductance $\sigma_1^{c,v}$ (blue), $\sigma_2^{c,v}$ (red), $\sigma_3^{c,v}$ (green), and σ_t (orange) as a function of E_F . Here, σ_t depicts the conductance contributed from all the bands, $\sigma_1^{c,v}$ depict the conductance contributed from the lowest conduction and highest valence bands, $\sigma_2^{c,v}$ depict the conductance contributed from the second lowest conduction and second highest valence bands, and so on. The solid black line corresponds to $\sigma = e^2/2h$. In (a) and (d), the yellow and light blue regions correspond to the magnetic gap on the top and bottom surfaces, respectively. (b, e) and (c, f) are the same as (a, d), except that they depict the semi-magnetic topological insulator phase and the Chern insulator phase, respectively. (g) Probability distribution as a function of layer index z for the highest valence band of the axion insulator phase for different k_x . (h) and (i) are the same as (a), except that they depict the second and third valence bands. The wave function distributions of the semi-magnetic topological insulator phase and the Chern insulator phase are similar to the axion insulator phase. We take $\Delta_t = 0.05$ for the axion insulator phase, $\Delta_t = 0$ for the semi-magnetic topological insulator phase, and $\Delta_t = -0.05$ for the Chern insulator phase. The Zeeman splitting term for the bottom surface is $\Delta_b = -0.1$ for all three phases. The film thickness is taken as $n_z = 50$.

of Δ_t for different thicknesses n_z . Though the energy difference decreases with the increasing film thickness, the first and second valence bands are still well separated in energy scale, as long as $\Delta_t \neq \pm\Delta_b$.

Moreover, we consider the case for $\Delta_b = -0.1$. The first row in Fig. 7 shows the spectra of the three topological phases, which are similar to those shown in the second row in Fig. 1, except that the high energies for

the first and second highest valence and lowest conduction bands merge into the bulk. This can be observed more clearly in the third row in Fig. 7, which shows the probability distributions of the first, second, and third highest valence bands, respectively. Thus, the probability distribution of the highest valence band at high energy with $k_x = \pi$ can be localized not only at the surface [the red lines in Figs. 2(a) and 6(a)], but also at the bulk [the red line in Fig. 7(g)]. Moreover, by checking the Hall conductance (the second row in Fig. 7), the probability distributions of the state at high energy will not change the fact that the Hall conductance is dominated by the lowest conduction and highest valence bands, when the Fermi energy resides inside the magnetic gap.

IX. CONCLUSION

In this work, we have investigated the energy spectra, wave function distribution, and the corresponding Berry curvature in the three distinct topological phases in magnetic topological insulator films, including the axion insulator phase, the semi-magnetic topological insulator phase, and the Chern insulator phase. In the axion and Chern insulator phases, a nearly half-quantized Hall conductance is observed at low energy near Γ point for the gapped Dirac cone (which is in accordance with the previous consensus), however, another nearly half-quantized Hall conductance must be compensated at high energy away from Γ point to ensure that the total Hall conductance is an integer-quantized number in units of e^2/h . In

the semi-magnetic topological insulator phase, the gapless Dirac cone hosts a vanishing Hall conductance at low energy near Γ point as expected, however, another half-quantized Hall conductance emerges at high energy away from Γ point. This explains how the contradiction between the previous consensus based on the low-energy effective model and the scenarios based on a lattice model is reconciled. Moreover, due to the coupling between the low-energy state and the high-energy state, the exact half quantization is only revealed in the gapless surface state in the semi-magnetic topological insulator phase, but not found in the gapped surface state in the axion and Chern insulator phases from the band calculation.

On the other hand, we adopt the layer-resolved Hall conductance to characterize the three phases. The half-quantized surface Hall effect is revealed in the three topological phases and it is contributed by all the occupied bands. This is distinct to the previous consensus that the half quantization originates from the individual gapped band.

ACKNOWLEDGMENTS

We thank helpful discussions with Bo Fu and Huan-Wen Wang. This work was supported by the Research Grants Council, University Grants Committee, Hong Kong under Grant Nos. C7012-21G and 17301220 and the National Key R&D Program of China under Grant No. 2019YFA0308603.

* sshen@hku.hk

¹ X.-L. Qi, T. L. Hughes, and S.-C. Zhang, “Topological field theory of time-reversal invariant insulators”, *Phys. Rev. B* **78**, 195424 (2008).

² K. Nomura and N. Nagaosa, “Surface-quantized anomalous hall current and the magnetoelectric effect in magnetically disordered topological insulators”, *Phys. Rev. Lett.* **106**, 166802 (2011).

³ X.-L. Qi and S.-C. Zhang, “Topological insulators and superconductors”, *Rev. Mod. Phys.* **83**, 1057 (2011).

⁴ F. D. M. Haldane, “Model for a quantum hall effect without landau levels: Condensed-matter realization of the “parity anomaly””, *Phys. Rev. Lett.* **61**, 2015 (1988).

⁵ L. Fu, C. L. Kane, and E. J. Mele, “Topological insulators in three dimensions”, *Phys. Rev. Lett.* **98**, 106803 (2007).

⁶ A. J. Niemi and G. W. Semenoff, “Axial-anomaly-induced fermion fractionization and effective gauge-theory actions in odd-dimensional space-times”, *Phys. Rev. Lett.* **51**, 2077 (1983).

⁷ R. Jackiw, “Fractional charge and zero modes for planar systems in a magnetic field”, *Phys. Rev. D* **29**, 2375 (1984).

⁸ G. W. Semenoff, “Condensed-matter simulation of a three-dimensional anomaly”, *Phys. Rev. Lett.* **53**, 2449 (1984).

⁹ R. S. K. Mong, A. M. Essin, and J. E.

Moore, “Antiferromagnetic topological insulators”, *Phys. Rev. B* **81**, 245209 (2010).

¹⁰ F. Wilczek, “Two applications of axion electrodynamics”, *Phys. Rev. Lett.* **58**, 1799 (1987).

¹¹ A. M. Essin, J. E. Moore, and D. Vanderbilt, “Magnetoelectric polarizability and axion electrodynamics in crystalline insulators”, *Phys. Rev. Lett.* **102**, 146805 (2009).

¹² M. Z. Hasan and C. L. Kane, “Colloquium: Topological insulators”, *Rev. Mod. Phys.* **82**, 3045 (2010).

¹³ J. Wang, B. Lian, X.-L. Qi, and S.-C. Zhang, “Quantized topological magnetoelectric effect of the zero-plateau quantum anomalous Hall state”, *Phys. Rev. B* **92**, 081107(R) (2015).

¹⁴ N. Varnava and D. Vanderbilt, “Surfaces of axion insulators”, *Phys. Rev. B* **98**, 245117 (2018).

¹⁵ B. Fu, Z.-A. Hu, and S.-Q. Shen, “Bulk-hinge correspondence and three-dimensional quantum anomalous Hall effect in second-order topological insulators”, *Phys. Rev. Research* **3**, 033177 (2021).

¹⁶ R.-L. Chu, J. Shi, and S.-Q. Shen, “Surface edge state and half-quantized Hall conductance in topological insulators”, *Phys. Rev. B* **84**, 085312 (2011).

¹⁷ Z. Liu, D. Qian, Y. Jiang, and J. Wang, “Dissipative edge transport in disordered axion insulator films”, *arXiv:2109.06178* (2021).

- ¹⁸ H.-P. Sun, C. M. Wang, S.-B. Zhang, R. Chen, Y. Zhao, C. Liu, Q. Liu, C. Chen, H.-Z. Lu, and X. C. Xie, “Analytical solution for the surface states of the antiferromagnetic topological insulator MnBi_2Te_4 ”, *Phys. Rev. B* **102**, 241406(R) (2020).
- ¹⁹ S.-Q. Shen, *Topological Insulators* (Springer Singapore, 2017).
- ²⁰ W.-Y. Shan, H.-Z. Lu, and S.-Q. Shen, “Effective continuous model for surface states and thin films of three-dimensional topological insulators”, *New J. Phys.* **12**, 043048 (2010).
- ²¹ H.-Z. Lu, A. Zhao, and S.-Q. Shen, “Quantum transport in magnetic topological insulator thin films”, *Phys. Rev. Lett.* **111**, 146802 (2013).
- ²² M. Mogi, Y. Okamura, M. Kawamura, R. Yoshimi, K. Yasuda, A. Tsukazaki, *et al.*, “Experimental signature of the parity anomaly in a semi-magnetic topological insulator”, *Nat. Phys.* **18**, 390 (2022).
- ²³ A. Gao, Y.-F. Liu, C. Hu, J.-X. Qiu, C. Tzschaschel, B. Ghosh, *et al.*, “Layer Hall effect in a 2D topological axion antiferromagnet”, *Nature* **595**, 521 (2021).
- ²⁴ M. Mogi, M. Kawamura, A. Tsukazaki, R. Yoshimi, K. S. Takahashi, M. Kawasaki, and Y. Tokura, “Tailoring tricolor structure of magnetic topological insulator for robust axion insulator”, *Sci. Adv.* **3**, eaao1669 (2017).
- ²⁵ Y.-J. Hao, P. Liu, Y. Feng, X.-M. Ma, E. F. Schwier, M. Arita, *et al.*, “Gapless surface Dirac cone in antiferromagnetic topological insulator MnBi_2Te_4 ”, *Phys. Rev. X* **9**, 041038 (2019).
- ²⁶ J.-Y. Zou, B. Fu, H.-W. Wang, Z.-A. Hu, and S.-Q. Shen, “Half-quantized hall effect and power law decay of edge-current distribution”, *Phys. Rev. B* **105**, L201106 (2022).
- ²⁷ J.-Y. Zou, R. Chen, B. Fu, H.-W. Wang, Z.-A. Hu, and S.-Q. Shen, “Half-quantized hall effect at the parity-invariant fermi surface”, *Phys. Rev. B* **107**, 125153 (2023).
- ²⁸ B. Fu, J.-Y. Zou, Z.-A. Hu, H.-W. Wang, and S.-Q. Shen, “Quantum Anomalous Semimetals”, *npj Quantum Materials* **7**, 94 (2022).
- ²⁹ R. Yu, W. Zhang, H.-J. Zhang, S.-C. Zhang, X. Dai, and Z. Fang, “Quantized anomalous hall effect in magnetic topological insulators”, *Science* **329**, 61 (2010).
- ³⁰ C. Chang, J. Zhang, X. Feng, J. Shen, Z. Zhang, M. Guo, *et al.*, “Experimental observation of the quantum anomalous hall effect in a magnetic topological insulator.”, *Science* **340**, 167 (2013).
- ³¹ C.-Z. Chang, W. Zhao, D. Y. Kim, H. Zhang, B. A. Assaf, D. Heiman, S.-C. Zhang, C. Liu, M. H. W. Chan, and J. S. Moodera, “High-precision realization of robust quantum anomalous hall state in a hard ferromagnetic topological insulator”, *Nat. Mater.* **14**, 473 (2015).
- ³² M. Mogi, R. Yoshimi, A. Tsukazaki, K. Yasuda, Y. Kozuka, K. S. Takahashi, M. Kawasaki, and Y. Tokura, “Magnetic modulation doping in topological insulators toward higher-temperature quantum anomalous Hall effect”, *Appl. Phys. Lett.* **107**, 182401 (2015).
- ³³ M. Mogi, M. Kawamura, R. Yoshimi, A. Tsukazaki, Y. Kozuka, N. Shirakawa, K. S. Takahashi, M. Kawasaki, and Y. Tokura, “A magnetic heterostructure of topological insulators as a candidate for an axion insulator”, *Nat. Mater.* **16**, 516 (2017).
- ³⁴ D. Xiao, J. Jiang, J.-H. Shin, W. Wang, F. Wang, Y.-F. Zhao, *et al.*, “Realization of the axion insulator state in quantum anomalous Hall sandwich heterostructures”, *Phys. Rev. Lett.* **120**, 056801 (2018).
- ³⁵ Y. Tokura, K. Yasuda, and A. Tsukazaki, “Magnetic topological insulators”, *Nature Rev. Phys.* **1**, 126 (2019).
- ³⁶ Y. Zhao, C.-Z. Chang, Y. Jiang, A. DaSilva, Y. Sun, H. Wang, *et al.*, “Demonstration of surface transport in a hybrid $\text{Bi}_2\text{Se}_3/\text{Bi}_2\text{Te}_3$ heterostructure”, *Sci. Rep.* **3**, 3060 (2013).
- ³⁷ K. M. Fijalkowski, N. Liu, M. Hartl, M. Winnerlein, P. Mandal, A. Coschizza, *et al.*, “Any axion insulator must be a bulk three-dimensional topological insulator”, *Phys. Rev. B* **103**, 235111 (2021).
- ³⁸ H. Li, H. Jiang, C.-Z. Chen, and X. C. Xie, “Critical behavior and universal signature of an axion insulator state”, *Phys. Rev. Lett.* **126**, 156601 (2021).
- ³⁹ Z. Liu and J. Wang, “Anisotropic topological magnetoelectric effect in axion insulators”, *Phys. Rev. B* **101**, 205130 (2020).
- ⁴⁰ H. Zhou, H. Li, D.-H. Xu, C.-Z. Chen, Q.-F. Sun, and X. C. Xie, “Transport theory of half-quantized hall conductance in a semimagnetic topological insulator”, *Phys. Rev. Lett.* **129**, 096601 (2022).
- ⁴¹ J. Liu and T. Hesjedal, “Magnetic topological insulator heterostructures: A review”, *Advanced Materials* , 2102427 (2021).
- ⁴² Y. Deng, Y. Yu, M. Z. Shi, Z. Guo, Z. Xu, J. Wang, X. H. Chen, and Y. Zhang, “Quantum anomalous Hall effect in intrinsic magnetic topological insulator MnBi_2Te_4 ”, *Science* **367**, 895 (2020).
- ⁴³ R.-X. Zhang, F. Wu, and S. Das Sarma, “Möbius insulator and higher-order topology in $\text{MnBi}_{2n}\text{Te}_{3n+1}$ ”, *Phys. Rev. Lett.* **124**, 136407 (2020).
- ⁴⁴ M. Z. Shi, B. Lei, C. S. Zhu, D. H. Ma, J. H. Cui, Z. L. Sun, J. J. Ying, and X. H. Chen, “Magnetic and transport properties in the magnetic topological insulators $\text{MnBi}_2\text{Te}_4(\text{Bi}_2\text{Te}_3)_n$ ($n = 1, 2$)”, *Phys. Rev. B* **100**, 155144 (2019).
- ⁴⁵ E. D. L. Rienks, S. Wimmer, J. Sánchez-Barriga, O. Caha, P. S. Mandal, J. Ruzicka, *et al.*, “Large magnetic gap at the dirac point in $\text{Bi}_2\text{Te}_3/\text{MnBi}_2\text{Te}_4$ heterostructures”, *Nature* **576**, 423 (2019).
- ⁴⁶ M. M. Otrokov, I. P. Rusinov, M. Blanco-Rey, M. Hoffmann, A. Y. Vyazovskaya, S. V. Eremeev, A. Ernst, P. M. Echenique, A. Arnau, and E. V. Chulkov, “Unique thickness-dependent properties of the van der Waals interlayer antiferromagnet MnBi_2Te_4 films”, *Phys. Rev. Lett.* **122**, 107202 (2019).
- ⁴⁷ W. Lin, Y. Feng, Y. Wang, Z. Lian, H. Li, Y. Wu, *et al.*, “Influence of the dissipative topological edge state on quantized transport in MnBi_2Te_4 ”, *Phys. Rev. B* **105**, 165411 (2022).
- ⁴⁸ Y. Li, C. Liu, Y. Wang, Z. Lian, H. Li, Y. Wu, J. Zhang, and Y. Wang, “Nonlocal Transport and One-dimensional Conduction in the Axion Insulator State of MnBi_2Te_4 ”, *arXiv:2105.10390* (2021).
- ⁴⁹ J. Li, Y. Li, S. Du, Z. Wang, B.-L. Gu, S.-C. Zhang, K. He, W. Duan, and Y. Xu, “Intrinsic magnetic topological insulators in van der Waals layered MnBi_2Te_4 -family materials”, *Sci. Adv.* **5**, eaaw5685 (2019).
- ⁵⁰ H. Li, S.-Y. Gao, S.-F. Duan, Y.-F. Xu, K.-J. Zhu, S.-J. Tian, *et al.*, “Dirac surface states in intrinsic magnetic topological insulators EuSn_2As_2 and $\text{MnBi}_{2n}\text{Te}_{3n+1}$ ”, *Phys. Rev. X* **9**, 041039 (2019).
- ⁵¹ J. Li, C. Wang, Z. Zhang, B.-L. Gu, W. Duan, and Y. Xu, “Magnetically controllable topological quantum phase transitions in the antiferromagnetic topological in-

- insulator MnBi_2Te_4 ”, *Phys. Rev. B* **100**, 121103 (2019).
- ⁵² Y. Li, Z. Jiang, J. Li, S. Xu, and W. Duan, “Magnetic anisotropy of the two-dimensional ferromagnetic insulator MnBi_2Te_4 ”, *Phys. Rev. B* **100**, 134438 (2019).
- ⁵³ S. H. Lee, Y. Zhu, Y. Wang, L. Miao, T. Pillsbury, H. Yi, *et al.*, “Spin scattering and noncollinear spin structure-induced intrinsic anomalous Hall effect in antiferromagnetic topological insulator MnBi_2Te_4 ”, *Phys. Rev. Research* **1**, 012011 (2019).
- ⁵⁴ B. Chen, F. Fei, D. Zhang, B. Zhang, W. Liu, S. Zhang, *et al.*, “Intrinsic magnetic topological insulator phases in the Sb doped MnBi_2Te_4 bulks and thin flakes”, *Nature Commun.* **10**, 4469 (2019).
- ⁵⁵ Y. J. Chen, L. X. Xu, J. H. Li, Y. W. Li, H. Y. Wang, C. F. Zhang, *et al.*, “Topological electronic structure and its temperature evolution in antiferromagnetic topological insulator MnBi_2Te_4 ”, *Phys. Rev. X* **9**, 041040 (2019).
- ⁵⁶ Y.-R. Ding, D.-H. Xu, C.-Z. Chen, and X. C. Xie, “Hinged quantum spin Hall effect in antiferromagnetic topological insulators”, *Phys. Rev. B* **101**, 041404(R) (2020).
- ⁵⁷ M. M. Otrokov, I. I. Klimovskikh, H. Bentmann, D. Estyunin, A. Zeugner, Z. S. Aliev, *et al.*, “Prediction and observation of an antiferromagnetic topological insulator”, *Nature* **576**, 416 (2019).
- ⁵⁸ R. Chen, S. Li, H.-P. Sun, Q. Liu, Y. Zhao, H.-Z. Lu, and X. C. Xie, “Using nonlocal surface transport to identify the axion insulator”, *Phys. Rev. B* **103**, L241409 (2021).
- ⁵⁹ M. Gu, J. Li, H. Sun, Y. Zhao, C. Liu, J. Liu, H. Lu, and Q. Liu, “Spectral signatures of the surface anomalous hall effect in magnetic axion insulators”, *Nat. Commun.* **12**, 3524 (2021).
- ⁶⁰ C. Liu, Y. Wang, H. Li, Y. Wu, Y. Li, J. Li, K. He, Y. Xu, J. Zhang, and Y. Wang, “Robust axion insulator and Chern insulator phases in a two-dimensional antiferromagnetic topological insulator”, *Nat. Mater.* **19**, 522 (2020).
- ⁶¹ R. Chen, H.-P. Sun, M. Gu, C.-B. Hua, Q. Liu, H.-Z. Lu, and X. C. Xie, “Layer Hall effect induced by hidden Berry curvature in antiferromagnetic insulators”, *Natl. Sci. Rev.*, nwac140 (2022).
- ⁶² C. Lei and A. H. MacDonald, “Kerr, Faraday, and Magnetoelectric Effects in MnBi_2Te_4 Thin Films”, [arXiv:2303.14635](https://arxiv.org/abs/2303.14635) (2023).
- ⁶³ R. Mei, Y.-F. Zhao, C. Wang, Y. Ren, D. Xiao, C.-Z. Chang, and C.-X. Liu, “Electrically Controlled Anomalous Hall Effect and Orbital Magnetization in Topological Magnet MnBi_2Te_4 ”, [arXiv:2303.06204](https://arxiv.org/abs/2303.06204) (2023).
- ⁶⁴ T. Morimoto, A. Furusaki, and N. Nagaosa, “Topological magnetoelectric effects in thin films of topological insulators”, *Phys. Rev. B* **92**, 085113 (2015).
- ⁶⁵ X.-L. Qi, R. Li, J. Zang, and S.-C. Zhang, “Inducing a magnetic monopole with topological surface states”, *Science* **323**, 1184 (2009).
- ⁶⁶ J. Maciejko, X.-L. Qi, H. D. Drew, and S.-C. Zhang, “Topological quantization in units of the fine structure constant”, *Phys. Rev. Lett.* **105**, 166803 (2010).
- ⁶⁷ W.-K. Tse and A. H. MacDonald, “Giant magneto-optical Kerr effect and universal Faraday effect in thin-film topological insulators”, *Phys. Rev. Lett.* **105**, 057401 (2010).
- ⁶⁸ J. Yu, J. Zang, and C.-X. Liu, “Magnetic resonance induced pseudoelectric field and giant current response in axion insulators”, *Phys. Rev. B* **100**, 075303 (2019).
- ⁶⁹ D. J. Thouless, M. Kohmoto, M. P. Nightingale, and M. den Nijs, “Quantized hall conductance in a two-dimensional periodic potential”, *Phys. Rev. Lett.* **49**, 405 (1982).
- ⁷⁰ H.-Z. Lu, W.-Y. Shan, W. Yao, Q. Niu, and S.-Q. Shen, “Massive Dirac fermions and spin physics in an ultrathin film of topological insulator”, *Phys. Rev. B* **81**, 115407 (2010).